

DOI: 10.1002/cphc.201200230

# High-Amplitude versus Low-Amplitude Current Oscillations during the Anodic Oxidation of *p*-Type Silicon in Fluoride Containing Electrolytes

Konrad Schönleber and Katharina Krischer<sup>\*[a]</sup>

Sustained electrochemical oscillations at *p*-type Si(100) in a dilute ammonium fluoride electrolyte are investigated by means of ellipsometric intensity and hydrogen measurements. Two main types of oscillations are identified, one with a low and one with a high current amplitude. It is demonstrated that the low-current amplitude oscillations do not involve any varia-

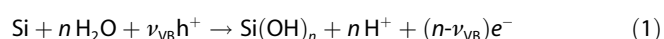
tions in oxide quality or etch rate. Furthermore, experimental results suggest that the high-amplitude current oscillations emerge from the low-amplitude current oscillations and thus share the feedback loops causing the oscillatory instability. Hence, the origin of oscillations during anodic dissolution of silicon has to be reconsidered.

## 1. Introduction

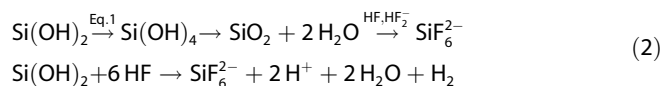
Current oscillations at *p*-Si electrodes are probably the most intensely investigated electrochemical oscillations.<sup>[1–12]</sup> Yet, the feedback loops necessary to produce the oscillatory instability are still disputed and although most authors agree that the oscillations are brought about by some change in oxide quality, the microscopic views as well as positive and negative feedback variables differ (for a concise discussion see ref. [13], chap. 5.10).

Herein, we present evidence that two fundamentally different oscillation types, one of them being unrelated to changes in oxide quality or etch rate, can be realized. This sheds new light on possible oscillation mechanisms.

The anodic electrochemical dissolution of silicon involves the electrochemical formation of an oxide layer and the etching of this oxide by fluoride species. The oxidation steps associated with a measurable current can be written as shown in Equation (1):



with  $n \in \{1, 2, 3, 4\}$  the total number of charge carriers transferred,  $\nu_{\text{VB}}$  the number of charge carriers transferred through valence band processes and  $(n - \nu_{\text{VB}})$ , consequently, the number of electrons injected into the conduction band. The electrochemical oxidation of the divalent intermediate  $\text{Si}(\text{OH})_2$  is in competition with its chemical oxidation accompanied by hydrogen evolution [Eq. (2)].<sup>[14,15]</sup>



The experimental means used to characterize the different oscillation types are ellipsometric intensity measurements (phase contrast-enhanced reflectivity) and measurements of the  $\text{H}_2$  production during the oscillations in an electrochemical flow cell.

## 2. Results

### 2.1. Oscillation Types

Upon a potential step from the open circuit potential (OCP) between  $-0.1$  and  $-0.05$  V versus the standard hydrogen electrode (SHE) to a potential of  $8.15$  V versus the SHE stable current oscillations at suitable external resistances are obtained. In this work we discern four different types of oscillations as depicted in Figure 1. The amplitude and frequency of the oscillations show a strongly varying behavior. Increasing the external resistance from the lowest values where oscillations are obtained ( $R_{\text{ext}} A \approx 2 \text{ k}\Omega \text{ cm}^2$ ), first the development of a shoulder at the decreasing slope of the previously sinusoidal oscillations with a relatively low amplitude (Figure 1 a, b) can be observed. If a threshold value of the external resistance of about  $R_{\text{ext}} A = 3.7 \text{ k}\Omega \text{ cm}^2$  is exceeded, the amplitude and also the frequency of the oscillations increase roughly by a factor of two (Figure 1 c). Upon further increase of the external resistance, resistance intervals, where these regular oscillations with a comparatively high amplitude are observed, and resistance intervals, where chaotic oscillations with a comparatively low amplitude (Figure 1 d) are observed, alternate. A phase space plot of the ellipsometric intensity versus the electrode potential  $\phi := U - R_{\text{ext}} A_j$  is shown in Figure 2. Figure 3 shows the change in the average current density and oscillations frequency depending on the external resistance. It can be concluded that the regular high-amplitude oscillations shown in Figure 1 c are strongly different from the other oscillation types. The difference of the oscillation types can be stressed further taking a look at the average current during the oscillations, compared to the current during a cyclic voltammogram with a slow scan

[a] K. Schönleber, Prof. Dr. K. Krischer  
Non-equilibrium Chemical Physics  
Physik-Department  
TU München  
James-Frank-Str. 1  
85748 Garching (Germany)  
E-mail: krischer@ph.tum.de

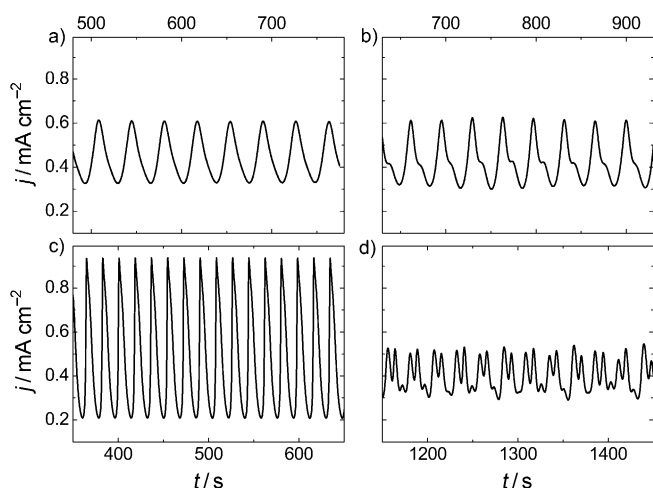


**Figure 1.** Different oscillation types at an applied potential of 8.15 V versus SHE with different external resistances in a 50 mM  $\text{NH}_4\text{F}$  solution (pH 2.3). a)  $R_{\text{ext}}A = 2.69 \text{ k}\Omega \text{ cm}^2$ , b)  $R_{\text{ext}}A = 3.59 \text{ k}\Omega \text{ cm}^2$ , c)  $R_{\text{ext}}A = 6.28 \text{ k}\Omega \text{ cm}^2$ , d)  $R_{\text{ext}}A = 7.30 \text{ k}\Omega \text{ cm}^2$ .

rate. This comparison is shown in Figure 4 together with the steady-state currents measured at different potentials  $\phi$  with  $R_{\text{ext}} = 0$ . While the low-amplitude current oscillations with and without a shoulder (Figure 1 a, b) are in good agreement with both the back-scan of the cyclic voltammogram and the steady-state measurements, the high-amplitude oscillations have a significantly higher average current density than expected. The average current densities of the chaotic oscillations agree with the cyclic voltammogram but not with the steady-state measurements. However, as they have not yet been studied intensely, they are not considered in the following sections.

## 2.2. Reaction Valency

In Figure 5, a positive scan of the *p*-Si working electrode is shown together with the hydrogen evolution, given as an equivalent current corrected for the collection efficiency of the Pt-wire. The current peak at the lowest potential ( $U_1$ ) corresponds to a strongly divalent ( $n=2$ ) dissolution of silicon as described in the Equations (1) and (2). Accordingly it is accompanied by pronounced  $\text{H}_2$  formation. Upon increasing the potential, first the hydrogen current sharply drops to a plateau around the second current peak at the silicon electrode ( $U_2$ ) and then drops further at potentials above 2 V versus the SHE. The oxidation steps described in

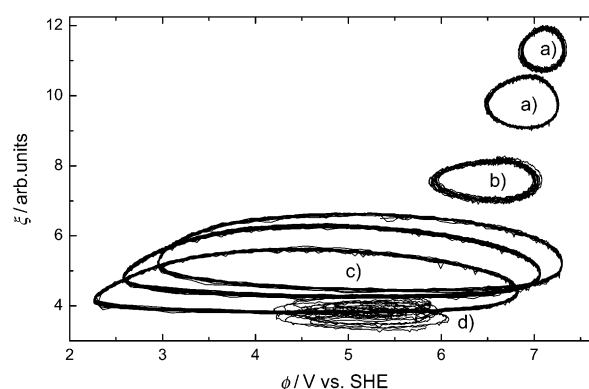


**Figure 2.** Ellipsometric intensity  $\xi$  versus electrode potential for different oscillation types. The letters refer to the oscillation types shown in Figure 1.

Equation (1) are strongly potential dependent whereas this dependency is less pronounced for the dissolution of divalent silicon species. This leads to the obtained overall decrease in the hydrogen current. The overall form of the hydrogen current depicted in Figure 5 is in good agreement with the values found in the literature.<sup>[3,15]</sup> The reaction valency  $\nu$  can be calculated directly from the  $\text{H}_2$  oxidation current at the Pt-wire,  $I_{\text{Pt}}$ , corrected for collection efficiency and time delay as described in Section 4.2, and the current at the silicon working electrode,  $I_{\text{Si}}$ , in the flow cell setup with Equation (3):<sup>[3]</sup>

$$\nu = \frac{4}{1 + \frac{I_{\text{Pt}}}{I_{\text{Si}}}} \quad (3)$$

The values found in our experiments are systematically larger than the literature values mentioned above, which can be ex-

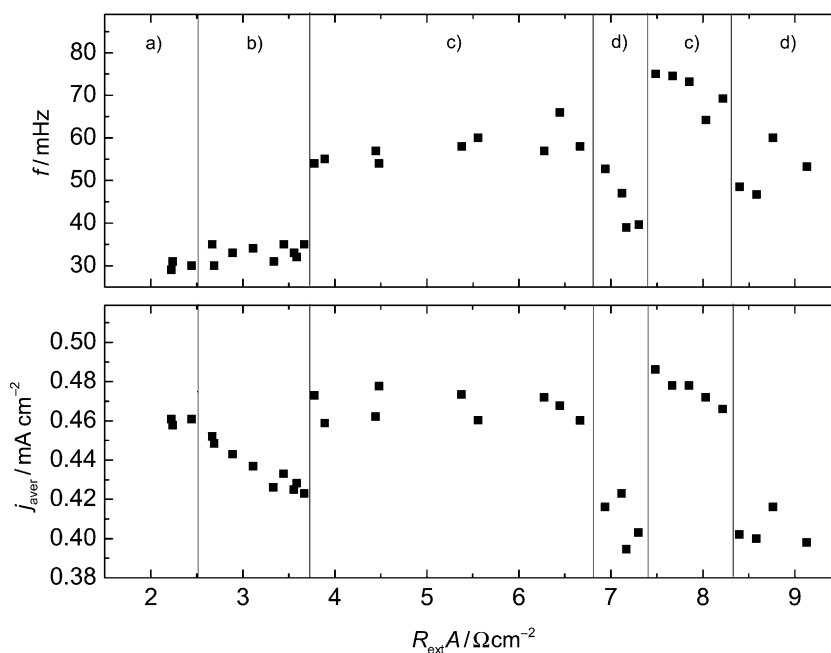


**Figure 3.** Oscillation base frequency (top) and average current density (bottom) during the current oscillations as a function of the external resistance  $R_{\text{ext}}$  multiplied by the sample area  $A$ .

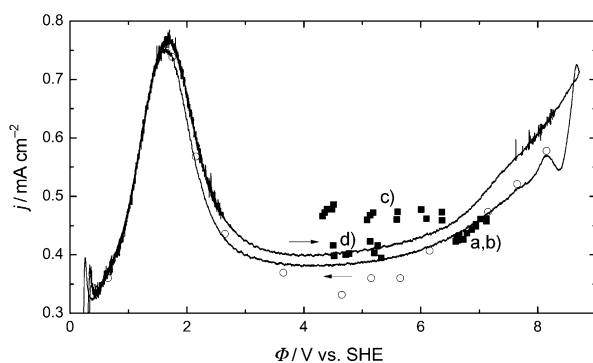


**Figure 4.** —: Cyclic voltammogram of a *p*-Si sample in a 50 mM  $\text{NH}_4\text{F}$  (pH 2.3) solution with a scan rate of  $5 \text{ mVs}^{-1}$ ; ○: steady-state currents ( $R_{\text{ext}}A=0 \text{ } \Omega\text{cm}^2$ ); ■: average current during the oscillations as a function of the average sample voltage. The letters refer to the different oscillations types shown in Figure 1.

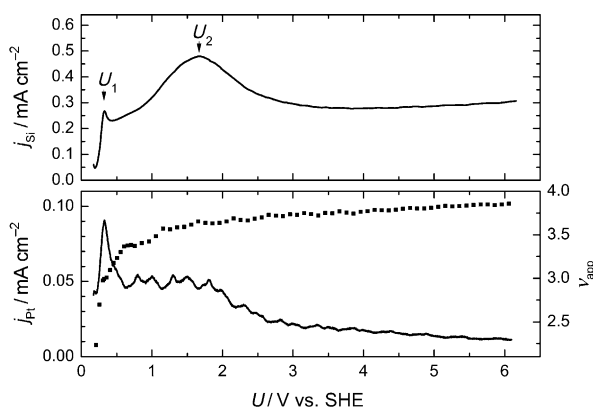


**Figure 5.** Positive voltage scan ( $5 \text{ mVs}^{-1}$ ) at *p*-Si electrode in a 50 mM  $\text{NH}_4\text{F}$  (pH 2.3) solution. Top: current density  $j_{\text{Si}}$  at the *p*-Si working electrode. Bottom: corresponding  $\text{H}_2$  oxidation current at Pt-wire corrected for collection efficiency normalized to the *p*-Si working electrode surface area (—) and reaction valency  $\nu$  (■).

plained by the lower  $\text{NH}_4\text{F}$  concentration used. This leads to a slower etch rate and thus suppresses the etching of the partially oxidized  $\text{Si}^{\text{II}}$  and correspondingly the  $\text{H}_2$  evolution.

### 2.2.1. Reaction Valencies during the Oscillations

Figure 6 depicts the reaction valencies during the oscillations. For all oscillation types except the high-amplitude current oscillations they are in good agreement with the expected values from the positive voltage scan in Figure 5 and the values for the electrode potentials during these oscillations shown in Figure 2. For these oscillation-types no oscillation of the  $\text{H}_2$  oxidation current above the noise limit can be seen. The regular high-amplitude oscillations (Figure 1c) show a different behavior, as the obtained  $\text{H}_2$  current is lower than expected for the potentials occurring during these oscillations. Only in this case is an oscillating hydrogen evolution seen as reported in the literature in ref. [3]. Interestingly, the same os-

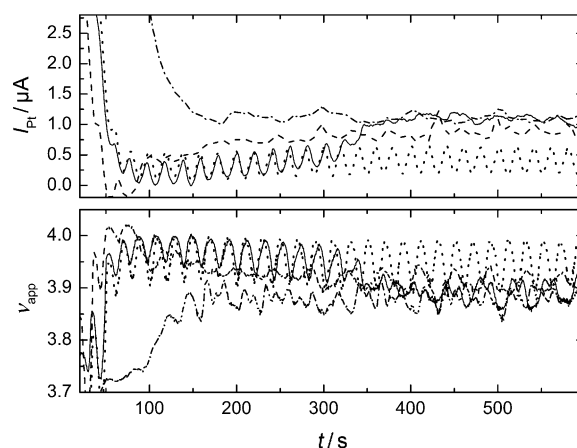


**Figure 6.** Top:  $\text{H}_2$  oxidation current at the Pt wire corrected for the collection efficiency during the turn-on transient and sustained current oscillation as shown in Figure 1a (----), Figure 1b (—), Figure 1c (••••) and Figure 1d (---). Bottom: corresponding reaction valency  $\nu$ .

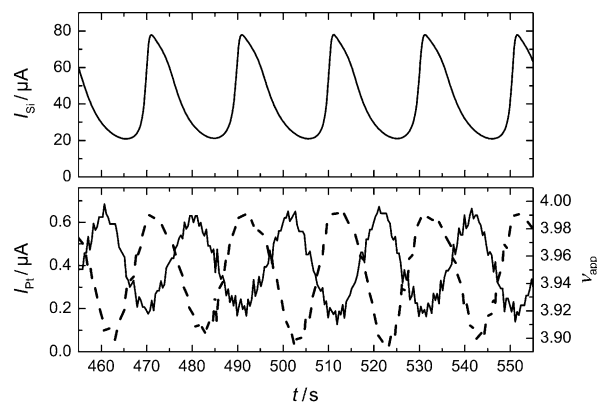


**Figure 7.** Top: silicon oxidation current at the *p*-Si working electrode. Bottom: corrected  $\text{H}_2$  oxidation current at the Pt-wire (—) and corresponding reaction valency (----).

cillatory behavior can be seen during the transient high-amplitude current oscillation preceding the sustained low-amplitude current oscillations with a shoulder (— in Figure 6). In Figure 7 the high-amplitude current oscillations are shown together with the  $\text{H}_2$  oxidation current. The time scale of the latter is corrected for the time delay between the silicon working electrode and the Pt-wire. From Figure 7 it can be concluded that the  $\text{H}_2$  evolution has the opposite phase of the current. A possible explanation is that during the relatively wide valleys of the current, where the electrode potential  $\phi$  is highest and comparable to the one of the low-amplitude current oscillations, as shown in Figure 2, the  $\text{H}_2$  evolution approaches the value of the low-amplitude current oscillations. Note that even in the case of the high-amplitude current oscillations, the resulting deviation in the reaction valency is very small and in the following analysis we assume a constant value of  $\nu=3.9$ .

## 2.3. Oxide Properties

### 2.3.1. Correlation between Current and Ellipsometric Intensity

As the current through the silicon surface exclusively leads to the production of  $\text{SiO}_2$  as seen in Equation (1), it is possible to quantify the mass of the silicon oxide produced by measuring the current, once  $\nu$  is found by the independent  $\text{H}_2$  measurement. At the same time, this silicon oxide is etched away leading to the following overall silicon oxide mass per unit area  $\mu$  [Eq. (4)]:<sup>[16]</sup>

$$\mu = \frac{M_{\text{SiO}_2}}{F\nu} \int_{t_0}^{t_1} j(\tau) d\tau - \int_{t_0}^{t_1} \mu_E(\tau) d\tau + \mu_{\text{av}} \quad (4)$$

Here,  $F$  is the Faraday constant,  $M_{\text{SiO}_2}$  the molar mass of the silicon oxide, and  $\nu$  the reaction valency, that is, the average number of charge carriers from the electrode leading to silicon oxidation.  $\mu_E$  is the etch rate and  $\mu_{\text{av}}$  the average silicon oxide-mass density per unit area. Note that we do not make any assumption for the oxide density as usually made in the literature,<sup>[6,10,17–19]</sup> as we argue later that the oxide density might change during the oscillations. At the same time the ellipsometric intensity is also a measure of the silicon oxide-mass density per unit area, which can therefore be written as shown in Equation (5):

$$\mu = c_{\text{opt}}(\tilde{\xi}) (\tilde{\xi} - \xi_0) =: c_{\text{opt}}(\tilde{\xi}) \cdot \tilde{\xi} \quad (5)$$

Here  $\tilde{\xi}$  is the measured ellipsometric intensity,  $c_{\text{opt}}(\tilde{\xi})$  is a parameter dependent on the details of the optical setup, and  $\xi_0$  is the value of the ellipsometric intensity with no silicon oxide at the surface. In any regime of sustained oscillations the time average of the etch rate per unit area  $\overline{\mu_E}$  is given by Equation (6):

$$\overline{\mu} = \frac{M_{\text{SiO}_2}}{F\nu} \cdot \frac{1}{t_1 - t_0} \int_{t_0}^{t_1} j(\tau) d\tau =: \frac{M_{\text{SiO}_2}}{F\nu} \cdot j_{\text{av}} \quad (6)$$

with  $t_1 - t_0$  being any integer multiple of the oscillation period. If additionally to a constant etch rate no significant variation of the optical parameter is assumed,  $c_{\text{opt}}(\xi_{\text{av}})$  can be determined using a least square fit (MATLAB). It is then used to fit the measured deviation of the ellipsometric intensity from the average value  $\xi(t) - \xi_{\text{av}}$  to the integral over the measured deviation of the current from the average current [Eq. (7)]:

$$c_{\text{opt}}(\xi_{\text{av}}) (\xi(t) - \xi_{\text{av}}) = \frac{M_{\text{SiO}_2}}{F\nu} \int_{t_0}^{t_1} j(\tau) - j_{\text{av}} d\tau \quad (7)$$

$$\Leftrightarrow c_{\text{opt}}(\xi_{\text{av}}) \cdot \xi(t) = c_{\text{opt}}(\xi_{\text{av}}) \cdot \xi_{\text{av}} + \frac{M_{\text{SiO}_2}}{F\nu} \int_{t_0}^{t_1} j(\tau) - j_{\text{av}} d\tau$$

### 2.3.2. Oxide Properties during the Oscillations

To directly test the quality of the silicon oxide in growth direction, etch-back experiments were performed. In these experiments the voltage was switched to the OCP at four different

oscillation phases, the maximum and minimum of both the ellipsometric intensity and the current. The decreasing curve of the ellipsometric intensity towards its minimal value  $\xi_0$  was recorded. Such etch-back curves for the oscillation types shown in Figure 1a–c together with their smoothed (Savitzky-Golay smooth, 4 s window) derivatives are shown in Figures 8–10.

In Figure 8 the shape of the etch-back curves  $\xi(t)$  and  $\dot{\xi}(t)$  is independent of the phase of the oscillation where the potential was turned off leading to the conclusion of a uniform quality of the silicon oxide layer for the low-amplitude current oscillations (Figure 1a). Clear variations of the etch-back curves with the turn-off phase can be seen in Figure 9 indicating slight changes in oxide quality for the low-amplitude current oscillations with a shoulder (Figure 1b). These variations are fully developed for the high-amplitude current oscillations (Fig-

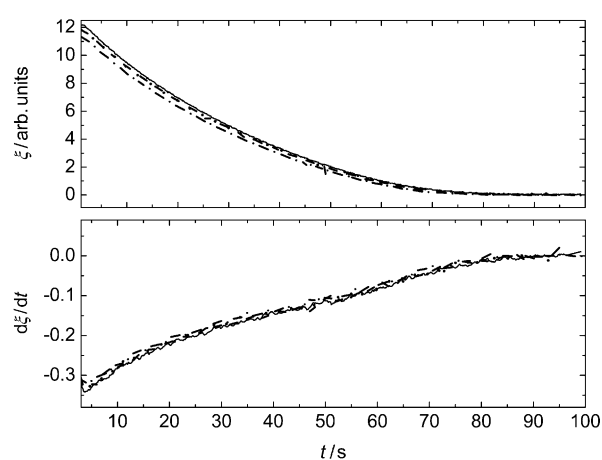


**Figure 8.** Etch-back curves for low-amplitude current oscillations as shown in Figure 1a Top: ellipsometric intensity  $\xi$  during etch-back started at maximal ellipsometric intensity (—), minimal ellipsometric intensity (---), maximal current (.....), minimal current (----). Bottom: time derivative of the etch-back curves.

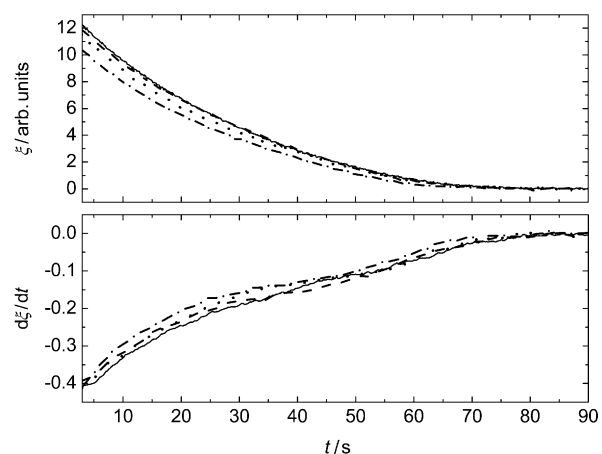


**Figure 9.** Etch-back curves for low-amplitude current oscillations with a shoulder as shown in Figure 1b Top: ellipsometric intensity  $\xi$  during etch-back started at maximal ellipsometric intensity (—), minimal ellipsometric intensity (---), maximal current (.....), minimal current (----). Bottom: time derivative of the etch-back curves.

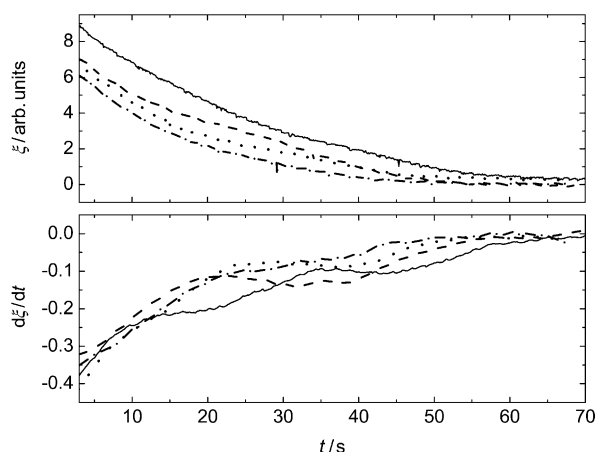


**Figure 10.** Etch-back curves for high-amplitude current oscillations as shown in Figure 1c. Top: ellipsometric intensity  $\xi$  during etch-back started at maximal ellipsometric intensity (—), minimal ellipsometric intensity (---), maximal current (.....), minimal current (-.-.-). Bottom: time derivative of the etch-back curves.

ure 1c). Here, the shape of the etch-back curves is strongly dependent on the phase of the oscillation where the potential is turned off. A non-uniform oxide quality in growth direction and thus density variations can be concluded.

During the low-amplitude current oscillations (Figure 1a, b) the amplitude of the potential variations is only about 10% as seen in Figure 2. Additionally, the optical parameter  $c_{\text{opt}}(\xi)$  is assumed to be constant, as the relative change in the ellipsometric intensity  $\xi$  is also below 10% (Figure 2) and changes in this parameter are expected to be small for this case.<sup>[20]</sup> Together with the assumption of a uniform oxide quality a constant etch rate during the oscillations is concluded. Under these assumptions the optical parameter of the average value of the ellipsometric intensity  $c_{\text{opt}}(\xi_{\text{av}})$ , and thus the value of the oxide mass per unit area  $\mu$ , can be calculated using Equation (7). The results of the fitting procedure are shown in Figures 11 and 12. For both oscillation types the fit is very good corroborating the assumption of a constant etch rate during the oscillations.

In contrast, for the high-amplitude current oscillations (Figure 1c) the fitting procedure does not yield a satisfying agreement of the oxide mass density per unit area obtained by ellipsometric intensity and current, respectively (Figure 13). Hence, the assumptions of a constant optical parameter  $c_{\text{opt}}(\xi)$  and a constant etching rate during the oscillations, do not hold in this case. Note that it is unlikely that the entire mismatch  $\Delta\mu$  can be attributed to variations of the optical parameter due to the phase mismatch between  $\Delta\mu$  ellipsometric signal. Therefore, a varying etch rate is to be assumed.

### 3. Discussion and Conclusions

Our experiments give evidence that oscillations in different parameter regimes involve different physico-chemical processes. The dynamic behavior during the anodic dissolution of silicon in fluoride containing electrolytes is thus even richer than pre-

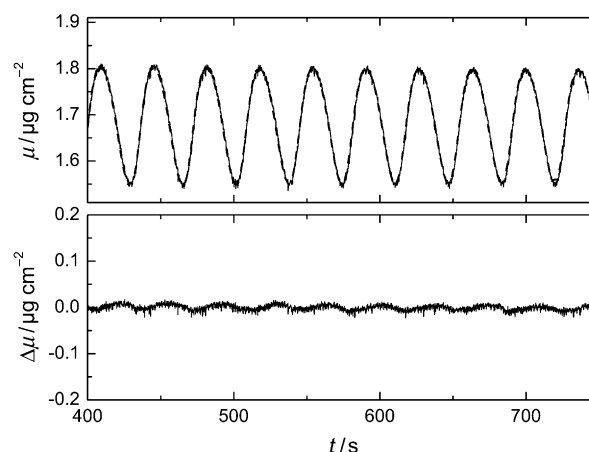


**Figure 11.** Top: silicon oxide-mass density  $\mu$  for low-amplitude current oscillations with shoulder as shown in Figure 1a calculated according to Equation (7) from the measured ellipsometric intensity (—) and the measured current (---), respectively. Bottom: difference  $\Delta\mu$  of the two curves in the top panel (to scale).

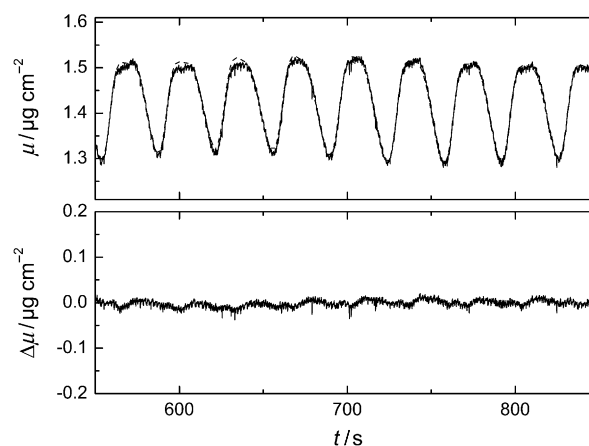


**Figure 12.** Top: silicon oxide-mass density  $\mu$  for low-amplitude current oscillations with shoulder as shown in Figure 1b calculated according to Equation (7) from the measured ellipsometric intensity (—) and the measured current (---), respectively. Bottom: difference  $\Delta\mu$  of the two curves in the top panel (to scale).

viously assumed (for a summary see ref. [13], chap. 5). Yet, the picture becomes also more structured. There are two main types of oscillations, the low-amplitude current oscillations (Figure 1a) and the high-amplitude current oscillations (Figure 1c). Their properties are summarized in Table 1.

The low-amplitude current oscillations occurring at larger values of the electrode potential  $\phi$ , do not involve different oxide qualities as seen in the etch-back curves in Figure 8, implying that the oxide-volume density remains constant during the oscillations. Additionally, the good agreement between oxide-mass-area density  $\mu$ , determined from the ellipsometric signal and from the integral of the current, substantiates the conclusion that the oxide is etched at a constant rate. Therefore, for these oscillations neither the etch rate nor the oxide density is an essential variable for the oscillation mechanism. As a consequence, it is also not the interplay between oxide



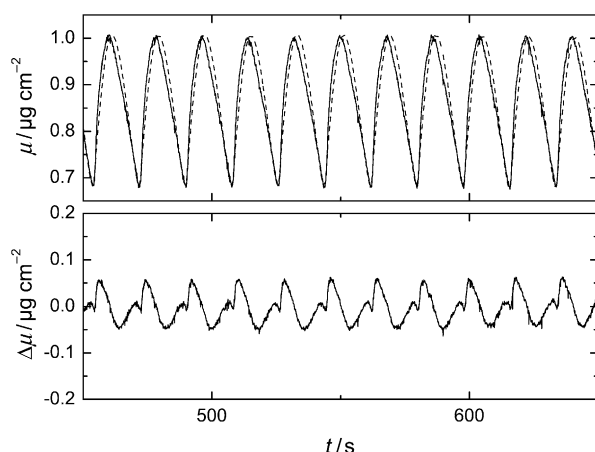


**Figure 13.** Top: silicon oxide-mass density  $\mu$  for low-amplitude current oscillations with shoulder as shown in Figure 1c calculated according to Equation (7) from the measured ellipsometric intensity (—) and the measured current (----). Bottom: difference  $\Delta\mu$  of the two curves in the top panel (to scale).

**Table 1.** Summary of oscillation properties differing for low- and high-amplitude current oscillations.

	Low amplitude	High amplitude
$\phi$ [V vs. SHE]	6–7.5	2–7.5
$j_{av}$	$\approx j_{fix\ point}$ at $R_{ext}=0$	$> j_{fix\ point}$ at $R_{ext}=0$
$f$	$f_0$ (ca. 30 mHz)	ca. $2f_0$
etch rate $\dot{\mu}_E$	constant	oscillating
oxide quality	uniform	nonuniform
$\nu$	constant (3.9)	oscillating (3.9–4)

formation and dissolution that causes the oscillations, and none of the mechanisms discussed in the literature seems to be applicable here.<sup>[5–7, 11, 17, 21–24]</sup> On the other hand, we know that the oscillations are only stable if there is a sufficiently large ohmic resistance in series to the interface, implying that electrical quantities are essential for the instability. One effect of the external resistance is that it modulates the potential drop across the interfacial region (semiconductor space-charge layer|oxide layer|Helmholtz layer) upon a change in the current density. This makes it likely that the driving force for the oscillations is in the electrical properties of the oxide layer, which change with potential  $\phi$  or the temporal change of potential  $d\phi/dt$  rather than composition or morphology of the oxide. Chazalviel showed that in the oxide is an excess of cations close to the Si|SiO<sub>2</sub> interface and an excess of anions close to the SiO<sub>2</sub>|electrolyte interface.<sup>[25]</sup> Different relaxation times upon a change in potential drop across the entire interface of the distinct charged regions could lie at the heart of the instability. Further studies in this direction are under way.

In contrast, the large amplitude oscillations involve different oxide qualities as well as different etch rates, as the etch-back experiments unambiguously show (Figure 10). Hence, these findings are in agreement with the literature reports mentioned above. The combined effect of both density variations and etch-rate changes give rise to the discrepancy between

the oxide-mass density determined from the ellipsometric signal and from the measured current (Figure 13). But owing to the fit procedure used, we can also learn from the difference signal that there is a phase shift between the oscillating oxide density and/or etch rate and the oxide-layer thickness. Therefore, at least one of the two quantities could constitute a true degree of freedom and might thus be essential for these oscillations. In contrast, the measured oscillations in the reaction valency  $\nu$  (Figure 7), besides being very small in amplitude, oscillate in antiphase to the oxidation current, and therefore  $\nu$  is unlikely to be a true variable in the oscillation mechanism.

Observe, however, that the large-amplitude current oscillations are not separated in phase space from the low-amplitude current oscillations. It is therefore possible that the primary instability is the same. This notion is underlined further by the occurrence of the low-amplitude current oscillation with a shoulder (Figure 1b) at intermediate values of  $R_{ext}A$ . These oscillations seem to mediate between low-amplitude and high-amplitude current oscillations sharing the relatively low amplitude and the base frequency with the former ones, while the first superharmonic component of the frequency, coinciding with the frequency of the latter ones, is already present. Furthermore, although the agreement between the mass density determined from the ellipsometric signal and the current is comparable to the low-amplitude current oscillations (Figure 12), the etch-back experiments reveal some variation in the oxide quality (Figure 9).

In conclusion, the high-amplitude current oscillations considered mostly in the literature so far seem to emerge from the low-amplitude current oscillations. A rational route towards an understanding of the interfacial nonlinear dynamics seems to proceed from the small-amplitude current oscillations to the high-amplitude current oscillations.

## Experimental

For all experiments single crystalline *p*-type silicon wafers (100) with a resistivity of 10–20  $\Omega\text{cm}$  were used. A thermally evaporated 200 nm aluminum layer annealed at 400 °C for 30 min under nitrogen atmosphere was used as an ohmic back contact.

The working electrode was cleaned by first cautiously rubbing it with an acetone (Merck, p.a.) drenched tissue and subsequently immersing it for 5 min each in acetone (Merck, p.a.), ethanol (Merck, p.a.), methanol (Merck, p.a.) and ultrapure Milli-Q millipore water (18.2  $\text{M}\Omega\text{cm}^{-1}$ ). After cleaning it was HF-etched for 3 min in 5% HF to achieve a reproducible and H-terminated surface. Care had to be taken not to destroy the HF soluble back contact.

All PTFE and platinum parts used were regularly cleaned with boiling piranha solution and were always stored in ultrapure water. An aqueous 1 M KOH solution was used to clean the glassware and the PMMA parts were first immersed in an aqueous solution of 1% KMnO<sub>4</sub> for several days and then cleaned of residual MnO<sub>2</sub> using 10% HCl in water. All parts were stored in covered ultrapure water baths to stay clean.

The electrolyte used for all experiments was an aqueous solution of 25 mM H<sub>2</sub>SO<sub>4</sub> (Merck, Suprapur) and 50 mM NH<sub>4</sub>F (Merck, p.a.).

Using literature values<sup>[26]</sup> for the dissociation constants of HF and H<sub>2</sub>SO<sub>4</sub>, we calculated the pH value to be 2.3.

### Ellipsometric Oxide Detection

For the ellipsometric silicon oxide detection the samples were fixed and electrically contacted with a conductive silver paste on a PTFE sample holder. Silicone rubber Scrintex 901 (Ralicks GmbH, Rees-Haldern, Germany) was used to seal the sample and the holder leaving an opening of 15–25 mm<sup>2</sup> in contact with the electrolyte. The assembled working electrode was then placed in a custom-made round PTFE cell together with a circular bent (diameter 5 cm) platinum wire (99.99%, Chempur) as the counter electrode and a Hg|Hg<sub>2</sub>SO<sub>4</sub> reference electrode.

Before the experiments the electrolyte was bubbled with argon constantly stirred at approximately 500 rpm with a magnetic stirrer for about 1 h. For the measurements the glass bubblers were removed to prevent an undefined change of the fluorine species concentration and an argon overpressure was maintained in the cell with an additional gas inlet. The stirring was retained during the experiments.

A potentiostat (FHI-2740, electronics laboratory of the Fritz-Haber-Institut, Berlin, Germany) was used for the potentiostatic control of the experiments and the current and voltage data were digitized using a data acquisition board (PCI-6221, National Instruments). A switchable resistor  $R_{\text{ext}}$  was placed between working electrode and potentiostat.

The optical path through the silicon oxide was measured with an ellipsometric microscope (Figure 14) using light from a blue LED ( $\lambda = 470$  nm) with an incident angle of  $\alpha = 70^\circ$  on the surface of the working electrode, elliptically polarized by a Glan–Thompson prism and a zeroth order  $\lambda/4$ -plate ( $\lambda = 488$  nm). The polarization

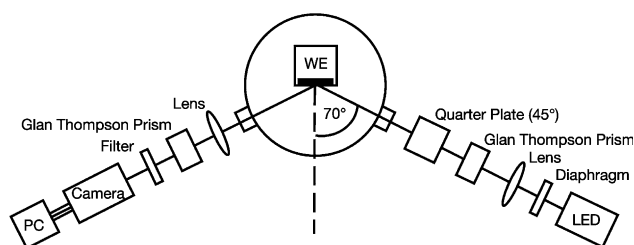


Figure 14. Optical setup of the custom-made ellipsometric microscope.

of the reflected light was then converted into an intensity signal by another Glan–Thompson prism as the analyzer. A lens was then used to create an image on an analog camera (JAI CV-A50) whose data were digitized by a frame grabber card (PCI-1405, National Instruments). The optical components were aligned with a microbench system (LINOS). A Labview program was used to acquire the data of the potentiostat and the camera simultaneously. No spatial inhomogeneity was observed during the experiments presented in this work confirming earlier results.<sup>[19]</sup> Consequently, only the spatial average of the ellipsometric intensity is presented here.

### H<sub>2</sub> Detection

For the hydrogen detection experiments a custom-made compact PMMA electrochemical flow cell was used. Here the *p*-Si working electrode was mounted using an FKM O-ring (diameter 4 mm) as

sealing. The electrolyte was constantly bubbled with argon in the reservoir above the working electrode, where also a glassy carbon rod (HTW GmbH, Thierhaupten, Germany) acting as the counter electrode was placed. For the measurements the electrolyte was drawn at a defined flow rate of 4  $\mu\text{L s}^{-1}$  from the reservoir past the working electrode and a platinum wire about 40  $\mu\text{L}$  downstream of the working electrode by a syringe pump (WPI, Berlin, Germany), resulting in a time delay between hydrogen production and detection of 10 s. The reference electrode (SCE) was also placed downstream of the working electrode to prevent IR distortions to the applied voltage, due to the relatively small cross-sectional areas of the flow channel combined with a significant electrolyte resistivity. The potential control of both the *p*-Si working electrode and the platinum electrode and the acquisition of the potentials and currents on both electrodes were realized with a PGU bipotentiostat (IPS, Münster, Germany). A switchable resistor  $R_{\text{ext}}$  was placed between the working electrode and the potentiostat.

The hydrogen produced at the working electrode was oxidized at the platinum wire at a potential of 200 mV versus SCE. The collection efficiency of the platinum wire was identified by measuring the H<sub>2</sub> oxidation current with a cathodic potential applied at the illuminated *p*-Si working electrode leading exclusively to H<sub>2</sub> formation there.<sup>[13]</sup> Before and after each measurement the current at the Pt-wire without hydrogen evolution at the working electrode was measured and the obtained values were then linearly interpolated as the background correction for the measurement in between.

### Acknowledgements

We thank Andreas Heinrich for providing the steady-state data given in Figure 4 and Kazuhiro Fukami for fruitful discussions. Financial support by the DFG (grant no. KR1189-12) and by the cluster of excellence "Nanosystems Initiative Munich" is gratefully acknowledged.

**Keywords:** ellipsometry • reaction valency • electrochemistry • semiconductors • silicon

- [1] D. R. Turner, *J. Electrochem. Soc.* **1958**, *105*, 402.
- [2] H. Gerischer, M. Lübke, *Ber. Bunsenges. Phys. Chem.* **1988**, *92*, 573.
- [3] D. J. Blackwood, A. Borazio, R. Greef, L. M. Peter, J. Stumper, *Electrochim. Acta* **1992**, *37*, 889–896.
- [4] J. N. Chazalviel, F. Ozanam, M. Etman, F. Paolucci, L. M. Peter, J. Stumper, *J. Electroanal. Chem.* **1992**, *327*, 343–349.
- [5] H. J. Lewerenz, M. Aggour, *J. Electroanal. Chem.* **1993**, *351*, 159–168.
- [6] M. Aggour, M. Giersig, H. J. Lewerenz, *J. Electroanal. Chem.* **1995**, *383*, 67–74.
- [7] V. Lehmann, *J. Electrochem. Soc.* **1996**, *143*, 1313.
- [8] J. Carstensen, R. Prange, G. S. Popkrov, H. Föll, *Appl. Phys. A* **1998**, *67*, 459.
- [9] F. Decker, E. Pantano, D. Dini, S. Cattarin, S. Maffi, G. Razzini, *Electrochim. Acta* **2000**, *45*, 4607–4613.
- [10] S. Böhm, L. M. Peter, G. Schlichthörl, R. Greef, *J. Electroanal. Chem.* **2001**, *500*, 178.
- [11] E. Foca, J. Carstensen, H. Föll, *J. Electroanal. Chem.* **2007**, *603*, 175.
- [12] H. Föll, M. Leisner, A. Cojocaru, J. Carstensen, *Electrochim. Acta* **2009**, *55*, 327–339.
- [13] X. G. Zhang, *Electrochemistry of Silicon and its Oxides*, Kluwer Academic, New York, **2001**.
- [14] R. Memming, G. Schwandt, *Surf. Sci.* **1966**, *4*, 109.
- [15] M. J. Eddowes, *J. Electroanal. Chem.* **1990**, *280*, 297.

- [16] Iljana Miethe. Spatio temporal pattern formation during the anodic electrodisolution of silicon in ammonium fluoride solution. PhD thesis, Technische Universität München, **2010** (<http://mediatum2.ub.tum.de/node?id=966027>).
- [17] J. N. Chazalviel, C. da Fonseca, F. Ozanam, *J. Electrochem. Soc.* **1998**, *145*, 964.
- [18] F. Yahyaoui, T. Dittrich, M. Aggour, J. N. Chazalviel, F. Ozanam, J. Rappich, *J. Electrochem. Soc.* **2003**, *150*, B205–B210.
- [19] I. Miethe, K. Krischer, *J. Electroanal. Chem.* **2012**, *666*, 1.
- [20] F. Linke, R. Merkel, *New J. Phys.* **2005**, *7*, 128.
- [21] J. Grzanna, H. Jungblut, H. J. Lewerenz, *J. Electroanal. Chem.* **2000**, *486*, 181.
- [22] J. Grzanna, H. Jungblut, H. J. Lewerenz, *J. Electroanal. Chem.* **2000**, *486*, 190.
- [23] H. J. Lewerenz, *J. Phys. Chem. B* **1997**, *101*, 2421.
- [24] S. Cattarin, F. Decker, D. Dini, *J. Phys. Chem. B* **1998**, *102*, 4779.
- [25] J. N. Chazalviel, *Electrochim. Acta* **1992**, *37*, 865.
- [26] S. Cattarin, I. Frateur, M. Musiani, B. Triboullet, *J. Electrochem. Soc.* **2000**, *147*, 3277.

---

Received: March 16, 2012

Published online on June 28, 2012

---